THE JOURNAL OF PHYSICAL CHEMISTRY C
A JOURNAL OF THE AMERICAN CHEMICAL SOCIETY

pubs.acs.org/JPCC

Article

Multiscale Catalyst Design for Steam Methane Reforming Assisted by Deep Learning

Changming Ke,[#] Weigang He,[#] Shixue Liu, Xiao Ru, Shi Liu,* and Zijing Lin*

Cite This: *J. Phys. Chem. C* 2021, 125, 10860−10867

Read Online

ABSTRACT: Computational design of high-quality catalysts targeting specific operation conditions is a challenging task due to the mechanistic, structural, and environmental complexities across multiple length and time scales. A multiscale method of a catalyst design linking *ab initio* calculations, microkinetics, and multiphysics modeling was proposed to address this challenge. The chemistry-based analytical model derived from a microkinetic model assisted by first-principles-based deep neural networks efficiently bridged zero Kelvin *ab initio* microscopic descriptors and multiphysics modeling. We applied the multiscale method to the design of carbon-resistant steam methane reforming catalysts, successfully identifying a few cost-efficient bimetallic alloys for CH_4 internal reforming solid oxide fuel cells. The multiphysics modeling demonstrates that catalysts of relatively low activity such as NiZn are actually beneficial for fuel efficiency, highlighting the importance of the multiphysics model for a multiscale computational catalyst design.

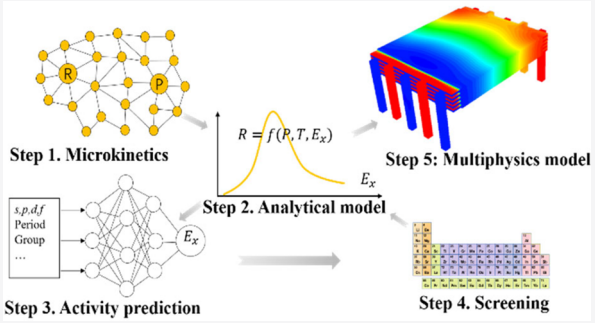

INTRODUCTION

Catalyst design is a complex, multidimensional, and multiscale task as the microscopic catalytical processes are intimately and dynamically coupled with evolving meso- to macroscopic environments in a reactor or an electrochemical cell.[1−3] In recent decades, the first-principles-based multiscale framework that combines *ab initio* calculations, microkinetics, and reactor modeling is emerging as a promising path to an advanced catalyst design under given operation conditions.[4−6] However, the implementation of a microkinetic model into a multiphysics model to fully couple the reaction network and various transport processes (e.g., heat, mass, and charge) in a reactor/cell[3] remains challenging and rarely reported. Moreover, time-consuming *ab initio* calculations of microscopic descriptors (such as adsorption energy) are the main bottleneck for high-throughput computational catalyst screening.

Recently, the energy scaling relation as the central concept for the design of descriptors of reactivity and selectivity has been combined with the *d*-band model to accelerate the search of new catalysts.[1,7] However, the *d*-band model is reasonably accurate only for a subset of alloy materials that have relatively small perturbations to the host metals.[8] Some machine learning augmented methods have been found to be capable of overcoming the limitation of the *d*-band model.[9−12] Adding features other than the *d*-band parameters as descriptors are found to improve the accuracy and predictive power of the machine learning method.[13−15] While the conventional machine learning methods show exceptional power in the catalyst design,[9−12] the exploration of those specially designed, sophisticated descriptive features is cumbersome and time-consuming. Moreover, these features are often too specific and non-universal. Deep neural networks (DNNs) have multiple hidden layers that allow the neural network to learn features of the data in a so-called feature hierarchy.[16] As simple features recombine from one layer to the next to form more complex features, the input features in DNNs can be simple and very general. DNNs have been widely applied to address questions such as crystal structure prediction and prediction of molecular excitation spectra.[17,18] In this work, we incorporate DNNs in a multiscale framework to realize cost-efficient materials screening.[19−21]

Here, a multiscale method merging top-down and bottom-up approaches was developed for the catalyst design, in which a chemistry-based analytical model serves as a crucial nexus efficiently bridging microscopic descriptors and multiphysics modeling, and first-principles-based deep neural networks (DNNs) were applied to rapidly predict needed descriptors. Using steam methane reforming (SMR) as an example, we first derived an analytical reaction rate equation based on a microkinetic model (top-down). Combined with the linear scaling relationship, the analytical model, without *a priori* assumption, clearly revealed that C* and O* adsorption

Received: February 23, 2021
Revised: April 14, 2021
Published: May 12, 2021

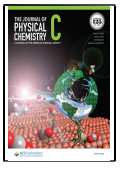

https://doi.org/10.1021/acs.jpcc.1c01632
J. Phys. Chem. C 2021, 125, 10860−10867

energies are key microscopic descriptors for experimental volcano plots and has explained seemingly a contradictory activity order of transition metals. To reduce the computational cost for first-principles-based high-throughput screening, we developed two DNNs that allow quick estimations of C* and O* adsorption energies using only basic elemental properties of bimetallic alloys. Three highly active, low-cost, coke-tolerant, and environment-friendly catalysts, Ni_3Ga, NiZn, and CoGa, were identified by screening through a large database of bimetallic alloys, and detailed DFT calculations further confirmed their catalytic performances. Finally, as the last step of the bottom-up approach to an industrial catalyst, the analytical model was implemented into a multiphysics model, which demonstrated that NiZn, though being less active, turned out to be a better catalyst for an internal reforming solid oxide fuel cell (SOFC).

WORKFLOW

We first illustrate the general workflow of the multiscale method for the catalyst design developed in this work. As shown in Figure 1, our starting point is an accurate

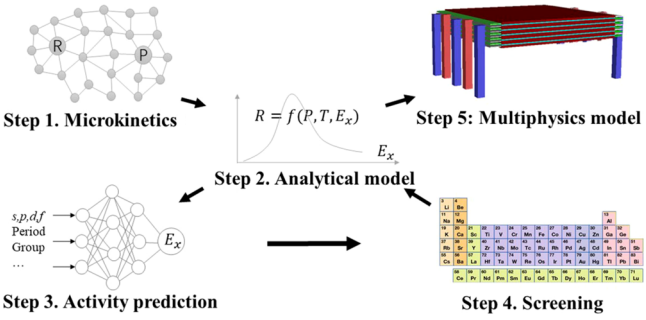

Figure 1. Schematic of the multiscale catalyst design merging top-down and bottom-up approaches.

microkinetic model based on adsorption energies computed with density functional theory (DFT) and rate constants estimated with the transition state theory. A rate equation is then derived from the microkinetic model, which leads to a simpler, thus more efficient analytical model that depends on microscopic descriptors (adsorption energies) without *ad hoc* assumptions. The validity of the model is confirmed by comparing experimental and theoretical reactivity volcano curves. DNNs trained from a database of DFT results are then developed for rapid predictions of adsorption energies. In the bottom-up approach to new catalysts, the high-throughput materials screening subjected to multiple practical constraints (e.g., costs and environmental friendliness) is carried out using the DNN-assisted analytical model. The identified catalysts are further tested in a multiphysics model, eventually leading to the best catalyst for considered operation conditions. The chemistry-based analytical model plays a central role in this multiscale method: it helps us to identify easily calculable descriptors in the top-down workflow while efficiently bridging zero Kelvin DFT quantities to working catalytic performances in a reactor or cell.

METHODS

DFT Calculations. DFT calculations were carried out with the plane wave computational software of the Vienna *ab initio* simulation package (VASP),[22−25] together with the exchange-correlation functional of OptB88-vdW.[26,27] The projector-augmented wave (PAW) method[28,29] was used to describe the electron−ion interaction between core ions and valence electrons. The wavefunctions of valence electrons were expanded in plane waves with an energy cutoff of 380 eV. A 3×3 unit cell with a three-layer slab and a vacuum region of 10 Å thick was used. The Brillouin zone was sampled by a $5 \times 5 \times 1$ Monkhorst−Pack k-point grid. All geometries were optimized using an energy-based conjugate gradient algorithm until the ionic energy was converged below 1×10^{-5} eV/atom and the electronic energy below 1×10^{-6} eV/atom. The climbing image nudged elastic band (CL-NEB)[30,31] and dimer[32] methods were used to find the minimum energy path and the transition state.

Database Building and Deep Learning. All binary alloys constituting 59 non-radiative metal elements with a 1:1 composition ratio combination were considered. The most stable structures of the $59 \times (59 - 1)/2 = 1711$ binary alloys were obtained from the Novel Materials Discovery (NOMAD) repository.[33] The largest portion of the structures, 400 out of 1711, belongs to the space group of 211 or the prototype of CsCl. This structure was therefore designated as the reference for the 1:1 binary alloy in this work, and these 400 alloys were used to construct the training database.

the adsorption energies of C* and O* on the low-energy, closest-packed (101) surfaces of the 400 alloys of the CsCl-type structure were calculated by considering the six possible adsorption sites, as shown in Figure 2. The training database

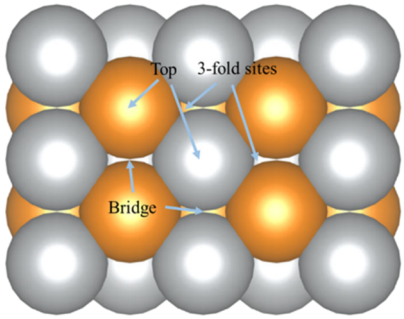

Figure 2. Six adsorption sites on the (101) surface of the CsCl prototype.

was then obtained by excluding anomalous results, i.e., due to highly distorted alloy surfaces or adsorbates moving inside the alloy or far away from the surface.

Considering the two adsorbates of C* and O* on six adsorption sites for each of the 400 alloys, there are a total of 4800 adsorption energy computations. Two types of calculations for each of the 400 adsorption cases were performed. The first assumed fixed positions for all alloy atoms. The second allowed the surface layer of the alloy to relax. Excluding the abnormal results described above, there were a total of, respectively, 2161 and 1973 data for the adsorption energies of C* and O* from calculations of the first type. The data set is referred to as data set 1. Similary, calculations of the second type lead to data set 2 containting 953 and 892 adsorption energies of C* and O*, respectively.

The DNN was built by the deep learning library of Keras running on TensorFlow.[34] After a large number of manual trial and error optimization of hyperparameters, the DNNs in this work used the following parameters: the number of neurons of

https://doi.org/10.1021/acs.jpcc.1c01632
J. Phys. Chem. C 2021, 125, 10860−10867

the input layer is 21, including 10 features for each of the two elements and the coordination number of the adsorption site; the 10 features of each element are the numbers of *s*-, *p*-, *d*-, and *f*-electrons, the first and second ionization potentials, the electron affinity, the covalent radius, the main valence state, and the row number of the element in the periodic table; there are eight hidden layers with a width of 20; to avoid overfitting, regularization methods, dropout and early stopping, were employed in our training, and the first hidden layer is a dropout layer with dropout rates of 0.2 and 0.3 for C* and O*, respectively; the activation function of the input and hidden layers is the exponential linear unit (ELU);[34] the output layer is a linear neuron that exports the adsorption energy of C* or O*; the mean absolute error (MAE) was used as the loss function; the optimization algorithm of AdaMax[35] was adopted; the learning rate is 0.004. When training the DNNs, the ratio of the training and validation data is 3:1, corresponding to 1621 (1480) adsorption energies as the training data and 540 (493) as the validation data for C* (O*) when trained in data set 1. The DNNs were first trained by data set 1 and then trained by data set 2. Furthermore, the C* and O* adsorption energies of all alloys were predicted using the average of 10 trained DNNs, and the lowest value of the six sites was selected.

Screening Criteria. All alloys were screened based on the criteria of activity, material cost, environmental friendliness, and stability in turn. First, only the alloys with SMR activity higher than that of Pd were picked. Second, for industrial applications, it is often necessary to limit the price of the catalyst. Therefore, the average price was used to estimate the cost of the alloy, assuming that the cost is independent of the preparation process but only depends on the cost of the constituted metals. Reference to the general cost of YSZ in a classic SOFC, alloys with the price exceeding $1400 per kg were abandoned. Third, to ensure environmental friendliness and safety, the alloys containing harmful heavy metals (such as Hg and Pb) were also excluded. Last, the ability of two elemental metals to form a stable alloy was considered. The stability was described by the alloy's formation energy E_f. The formation energy of an alloy was defined as

$$E_f = E_{alloy} - n_A E_A - n_B E_B$$

where E_{alloy} is the DFT calculation energy of the alloy and n_i and E_i (i = A and B) are the molar ratio and the DFT-calculated energy, respectively, of the individual metal i. According to this definition, the more negative the value, the more stable the alloy. In this work, only alloys with a formation energy of less than 0 eV per unit cell were considered to be potentially stable.

Multiphysics Model. This multiphysics model was constructed by the CFD software, FLUENT, supplemented with in-house developed external subroutines.[3,36] A 120 mm × 120 mm × 21.5 mm five-cell SOFC stack was built, fuel and air streams were separated by a solid region consisting of the typical positive electrode-electrolyte-negative electrode assembly in every cell of the stack, and every cell contained 30 fuel/air channels. This 3D model took into account the coupled physical processes of mass, charge, and heat transport, and chemical and electrochemical reactions. The velocity of the fuel inlet was 0.5 m/s, CH_4:H_2O was 3:1, the velocity of air flow was 2 m/s, and the temperature was 1023 K. The mesh independency is shown in Figure S1 in the Supporting Information, and the computational cost for the 3.8 million mesh used in this case is about 16 CPU hours. More details of the model geometry, boundary conditions, and governing equations can be found in our previous works.[3,36]

RESULTS AND DISCUSSION

Analytical Model Derived from Microkinetics. The microkinetics is generally based on dozens of elementary reactions.[37] The rate-limiting mechanism(s) was often concealed by the complex reaction network,[38] which obscures the knowledge of the reactions and hinders the rational catalyst design. Moreover, it is numerically challenging to couple dozens (even hundreds) of differential equations of a microkinetic model with a multiphysics model, preventing the performance prediction of catalysts in practical applications. So, a cost-efficient analytical model that captures the main chemistry of a microkinetic model is the key to the multiscale catalyst design.

A detailed study on the microkinetics involved in the SMR reaction was reported in our recent work,[37] and the major pathway that consisted of two rate-determining steps (CH_4 + 2* → CH_3* + H* and CH* + O* → CHO* + *) obtained by the flux analysis is

$$CH_4 \underset{k_{-1}}{\overset{k_1}{\rightleftarrows}} CH_3^* \Leftrightarrow CH_2^* \Leftrightarrow CH^* \overset{k_4}{\rightarrow} CHO^* \Leftrightarrow CO^* \Leftrightarrow CO \quad (1)$$

Here, ⇄ indicates a reversible step, ⇔ indicates a quasi-equilibrium step, and → indicates an irreversible step. Specifically, except for the CH_4 decomposition step (k_1/k_{-1}) and the CH* oxidation step (k_4), all the other steps can be considered at equilibrium. According to eq 1, the rate expression is (see derivations in eq S2)

$$r_{CH_4} = \frac{A_1 \exp\left(-\frac{E_1^a}{RT}\right) P_{CH_4}}{(1 + \gamma_{O^*} + \gamma_{CH^*})^2 (1 + \gamma_{R4})} \quad (2)$$

where

$$\gamma_{O^*} = A_{O^*} \exp\left(-\frac{E_{O^*}}{RT}\right) \frac{P_{H_2O}}{P_{H_2}}$$

and

$$\gamma_{CH^*} = \frac{1}{A_{CH^*} \exp\left(\frac{E_{CH^*}}{RT}\right) \frac{P_{H_2}^{3/2}}{P_{CH_4}} + A_{CH^*+O^*} \exp\left(\frac{E_1^a - E_4^a - E_{O^*}}{RT}\right) \frac{P_{H_2O}}{P_{H_2} P_{CH_4}}}$$

are the ratios of O* and CH* coverages to active sites, respectively. $\gamma_{R4} = A_4 \exp\left(\frac{E_{CH^*} + E_{O^*} + E_4^a - E_1^a}{RT}\right) \frac{P_{H_2}^{5/2}}{P_{H_2O}}$ quantifies the effect of the rate-determinig step of CH* oxidation. A is a T-dependent parameter, P_i is the pressure of gas i, E_m is the adsorption energy of species m, defined as $E_m = E_{m\_surf} - E_m - E_{surf}$, and E_n^a is the activation energy of reaction n. As shown in eq 2, the reaction rate of CH_4 is dependent on working conditions (e.g., temperatures, pressures, and gas compositions), two activation energies (E_1^a and E_4^a), and two adsorption energies (E_{O^*} and E_{CH^*}). So, the volcano relationship of the reaction rate with adsorption energies of C-based and O-based species is interpretable: a too strong adsorption of O* (CH*) will decrease the reaction rate due to the increased value of γ_{O^*} (γ_{CH^*}); low coverages of O* and CH* caused by weak

https://doi.org/10.1021/acs.jpcc.1c01632
J. Phys. Chem. C 2021, 125, 10860−10867

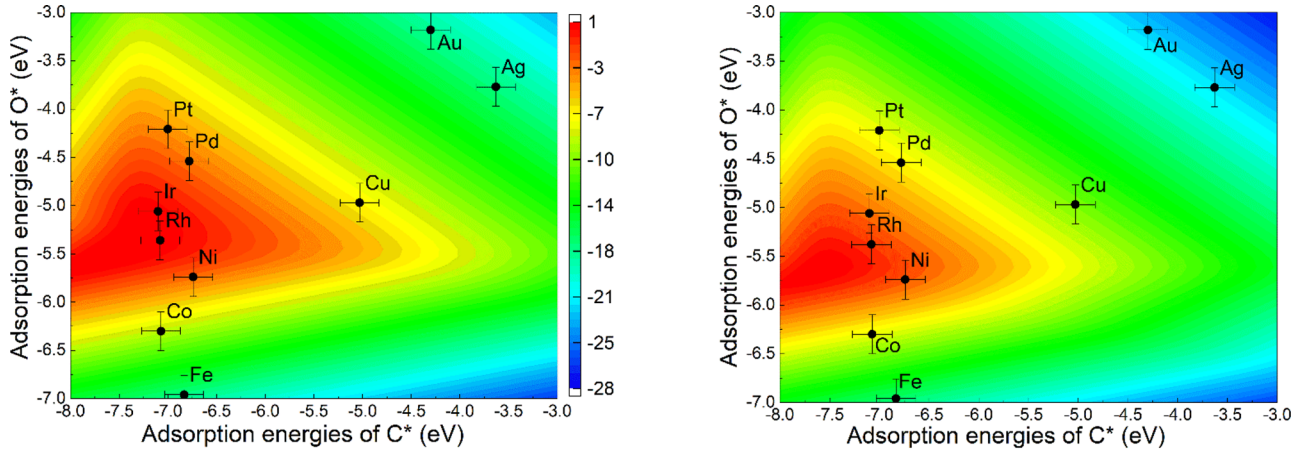

Figure 3. SMR activities as a function of C* and O* adsorption energies with the scale of $\log_{10}[r\mathrm{CH_4}(\mathrm{molecules/site/s})]$. All group VIII metals are face-centered cubic, except Co (hexagonal close-packed). SMR activities calculated at (a) T = 833 K, P_{H2O}:P_{CH4}:P_{H2} = 20:5:2 taken from ref 41. (b) T = 773 K, P_{H2O}:P_{CH4} = 3 taken from ref 42. The ordering of experimental SMR activities is Rh > Ir > Ni > Pd ∼ Pt in panel (a) and is Rh > Ni > Ir > Pd ∼ Pt ≫ Co ∼ Fe in panel (b).

adsorptions will also decrease the reaction rate, as reflected by the increased value of γ_{R4} in the denominator of eq 2. So, only catalysts with moderate adsorption energies of O* and CH* will exhibit great reactivity. According to the linear scaling relationship,[39,40] E_1^a, E_4^a, and E_{CH^*} can be linearly expressed by the adsorption energies of C* and O* (see Figure S2). Therefore, our simple yet rigorous analytical model naturally led to two microscopic descriptors for SMR catalytic activity.

We then used the analytical model to construct the volcano plot that compares the activity ordering of typical transition metals for SMR. It was found in experiments that the activity ordering of Ir and Ni depends on operation conditions sensitively.[41,42] Figure 3 shows the theoretical volcano plots of group VIII metals under two different experimental conditions, agreeing well with available experimental data. The analytical model offered an intuitive explanation of the condition-dependent activity ordering: a higher ratio of H_2O:CH_4 will drive the volcano top moving toward metals with weaker O* adsorption energies as too much H_2O will cause the flooding of surface O*. The experiment-theory agreement not only emphasized the necessity of a predictive condition-dependent model for the catalyst design but also validated the use of C* and O* adsorption energies as the descriptors for SMR activity.

Activity Prediction Assisted by Deep Learning. In this study, we focused on binary alloy $A_{0.5}B_{0.5}$ composed of metals A and B selected from 59 non-radiative metals. Even for this relatively simple composition, there are a total of 1711 alloys, requiring considerable computing resources for full *ab initio* calculations of descriptors. To address this issue, we constructed two DNNs that take in only basic element features (such as *s*-, *p*-, *d*-, and *f*-electrons) and output C* or O* adsorption energies. The mean absolute errors (MAEs) of the DNNs are 0.21 and 0.18 eV (the root mean square error is about 0.25 eV) for C* and O* adsorption energies, respectively, over an energy window from −10.0 to −1.0 eV, as shown inFigure S3 , indicating a satisfactory accuracy needed for high-throughput screening of the remaining alloys. In comparison, the predictive root mean square errors for CO and OH adsorption energies of a *d*-band-based machine learning model are about 0.22 and 0.24 eV, respectively, over a narrower energy window from −2 to 2 eV.[11] It is noted that the DNNs developed in this work only require the knowledge of basic element features yet still resulting in an accuracy comparable with other machine learning-based methods that require sophisticated feature engineering and/or time-consuming calculations of features (e.g., *d*-band properties).[10,11] We believe that current DNNs can be further improved to cover metal alloys over a wider composition range.

The DNN-predicted adsorption energies serve as inputs for the analytical model, allowing rapid estimations of activities of all $A_{0.5}B_{0.5}$ alloys under any given operation conditions. We show in Figure 4a the activity distribution of all binary alloys at a temperature of 600 °C, a flow pressure of 1 atm, a steam-methane ratio of 2:1, and a methane conversion of 50%. We found that 88 $A_{0.5}B_{0.5}$ alloys possess higher SMR activities than Pd, among which 90% of them contain group VIII metals with the rest of the alloys containing Mo, Cr, or Re. This finding is consistent with the general understanding that group VIII metals are good SMR catalysts.

Pursuit of Coke-Resistant Industrial Catalysts. The DNN-assisted analytical model identified dozens of highly active alloys. We further screened these new catalysts by considering other desirable properties for an industrial catalyst such as cost, environment friendliness, and stability. After other rounds of screening, seven alloys remain, i.e., CoGa, CoSn, CoZn, CoNi, NiZn, FeGa, and FeSn. The detailed screening process is listed in Table S1, and the activities of these alloys are highlighted in Figure 4a.

The coke deposition on conventional Ni-based catalysts is a well-known issue causing catalyst failure.[50] So, the coke resistance is also an essential feature of industrial SMR catalysts. Catalysts comprising SMR-active (Ni) and SMR-inactive (Au, Ag, and Cu) metals have proven to be coke-resistant.[51] Therefore, except for the CoNi alloy that consists of two SMR-active metals reportedly prone to carbon deposition,[52,53] the remaining binary alloys comprising one SMR-active metal (Fe, Co, and Ni) and one SMR-inactive (Zn, Ga, and Sn) metal are likely to be coke-resistant. As a reasonable extension, besides the six highly active catalysts

https://doi.org/10.1021/acs.jpcc.1c01632
J. Phys. Chem. C 2021, 125, 10860−10867

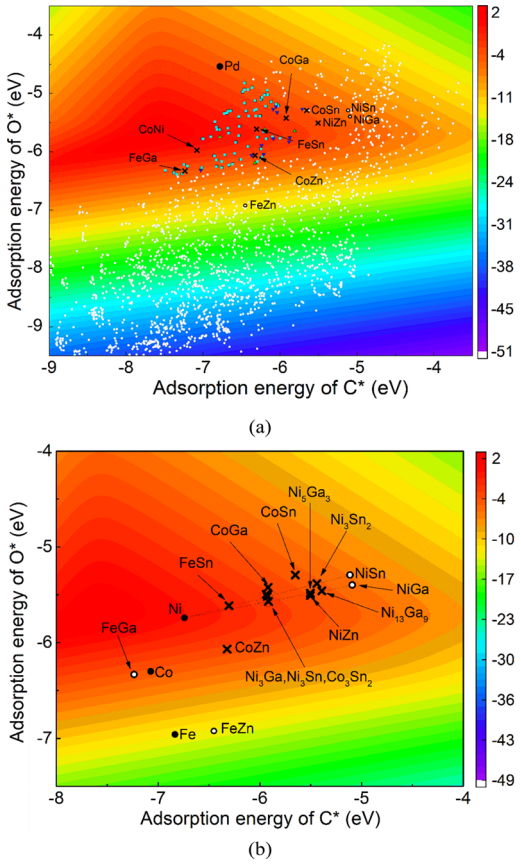

Figure 4. Alloy screening based on the DNN-assisted analytical model. The contour plot of SMR activity as a function of adsorption energies of C* and O* is calculated at a temperature of 600 °C, a flow pressure of 1 atm, a steam-methane ratio of 2:1, and a methane conversion of 50%. (a) Screening results of 1711 binary alloys. The black circle is the reference metal (Pd), and the crosses represent recommended alloys with desired properties for industrial catalysis. Alloys abandoned in the screening due to low activity (white circles), high cost (the cyan squares), containing heavy metals (blue lower triangles), and instability (green upper triangles) are also labeled. (b) Search alloys beyond the $A_{0.5}B_{0.5}$ composition with the activity interpolation method. The crosses represent high-activity alloys known in experiments: CoGa,[43] CoSn,[44] CoZn,[45] NiGa,[46] NiSn,[47] NiZn,[48] and FeSn.[49] Alloys less active than Pd are indicated by white circles with black edges.

(CoGa, CoSn, CoZn, CoNi, NiZn, FeGa, and FeSn) obtained directly from the screening, we also considered three complementary bimetallic alloys, NiSn, NiGa, and FeZn. In summary, the nine alloys constituted by (Fe, Co, and Ni) and (Zn, Ga, and Sn) were considered promising coke-resistant catalysts.

Our screening results are consistent with experimental observations. For example, the SMR catalytic activities of NiSn and NiZnAl and their abilities to resist carbon deposition have already been confirmed in experiments.[54−56] Additionally, there were reports demonstrating the activities of NiZn and NiGaMg in the hydrogenation of acetylene[57] and ethanol steam reforming,[58] respectively. These experiments are direct verifications of our multiscale catalyst design.

So far, we only focused on $A_{0.5}B_{0.5}$. Following ref 59, we further used an activity interpolation method to study binary alloys over a wider composition range based on the nine $A_{0.5}B_{0.5}$ alloys identified previously. Eleven binary alloys of high activity are found from existing phase diagrams,[43−49,60] as shown in Figure 4b. In particular, CoGa, NiZn, and Ni_3Ga possess wide ranges of homogeneity (the properties of alloy phases are summarized in the Table S2), suggesting an easy synthesis of these compounds,[61] and are also stable at high temperatures above 1000 °C.[43,46,48]

Reconfirmation with DFT. The SMR activity and coke resistance of CoGa, NiZn, and Ni_3Ga were confirmed by detailed DFT calculations using typical catalysts, Pb and Ni, as references. The catalytic activity depends on the oxidation of CH*, which is the rate-determining step of SMR. As shown in Figure 5a, the lower activity of Pt is caused by the higher activation energy (E_a) of CH* + O* → CHO*, and based on the value of E_a, the activity ordering follows CoGa (2.54 eV) ∼ Ni_3Ga (2.63 eV) ∼ Ni (2.67 eV) > NiZn (3.18 eV) > Pt (3.45 eV). On the other hand, the carbon tolerance of a catalyst depends on the activation energy of C_2 formation,[51] as shown in Figure 5b. We found that Pt is more resistant toward carbon deposition than Ni, agreeing with experiments.[41,62] The ordering of carbon resistance is CoGa (2.06 eV) ∼ NiZn (1.99 eV) ∼ Pt (1.94 eV) > Ni_3Ga (1.77 eV) > Ni (1.09 eV). Considering both activity and coke resistance, CoGa and Ni_3Ga are better catalysts than NiZn. However, as we will demonstrate below, the catalytic performance under operation conditions should also be accounted for when selecting the best catalyst.

Multiphysics Model. We found that the activity of NiZn is significantly lower than Ni, Ni_3Ga, and CoGa. Does this mean that the latter three catalysts are always better than NiZn? The answer is condition-dependent. The CH_4-fueled SOFC directly converts the chemical energy of CH_4 into electricity, in which SMR occurs in the anode. The internal reforming CH_4-fueled SOFC offers high energy conversion efficiency. As the final step of the multiscale catalyst design, we coupled the analytical model with a multiphysics model of the internal reforming SOFC stack, as shown in Figure 6a, to evaluate the performances of Ni and NiZn in actual conditions. As the activites of Ni_3Ga and CoGa are comparable with that of Ni, we expect that these two alloys will have performances similar to Ni.

Surprisingly, although the activity of NiZn is only 1% of Ni at 1023 K, the power density of the NiZn-catalyzed SOFC is about 20% higher than the Ni-catalyzed SOFC (Figure 6b). The outperformance of NiZn comes exactly from its relatively low activity. As shown in Figure 6c, the excessive reforming of CH_4 in the Ni-catalyzed SOFC stack adsorbed too much heat, and a strong endothermic zone formed near the fuel inlet such that the endothermic and exothermic areas are separated. Consequently, the electrochemical heat from the hydrogen oxidation cannot be used by endothermic SMR, which reduces the electricity output. In contrast, in the NiZn-catalyzed SOFC, as shown in Figure 6d, the lower SMR activity gives rise to a much smaller temperature gradient and thus a higher energy conversion efficiency. Moreover, a more uniform temperature distribution across the stack (from inlet to outlet) is beneficial for fuel cell stability and lifetime under practical conditions.[63] As a result of our multiscale catalyst design, NiZn is recommended as the catalyst for the internal reforming SOFC. These results highlight the importance of the multiscale catalyst design that incorporates multiphysics modeling.

https://doi.org/10.1021/acs.jpcc.1c01632
J. Phys. Chem. C 2021, 125, 10860−10867

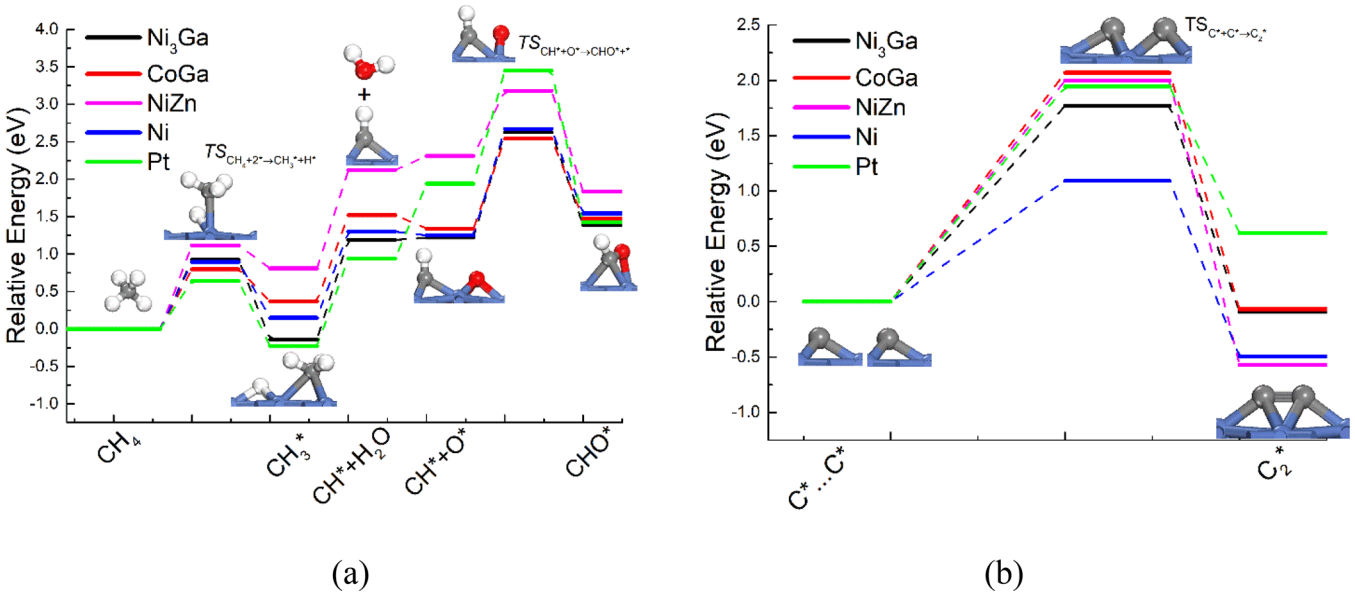

Figure 5. SMR activity (a) and carbon tolerance (b) on $Ni_3Ga(111)$, CoGa(110), NiZn(110), Ni(111), and Pt(111) based on DFT calculations. The H* in reaction CH* + H_2O → CH* + O* + 2H* is not shown in panel (a). C*···C* indicates two isolate C* adsorbates, and C* + C* indicates two carbons on two adjacent sites in panel (b).

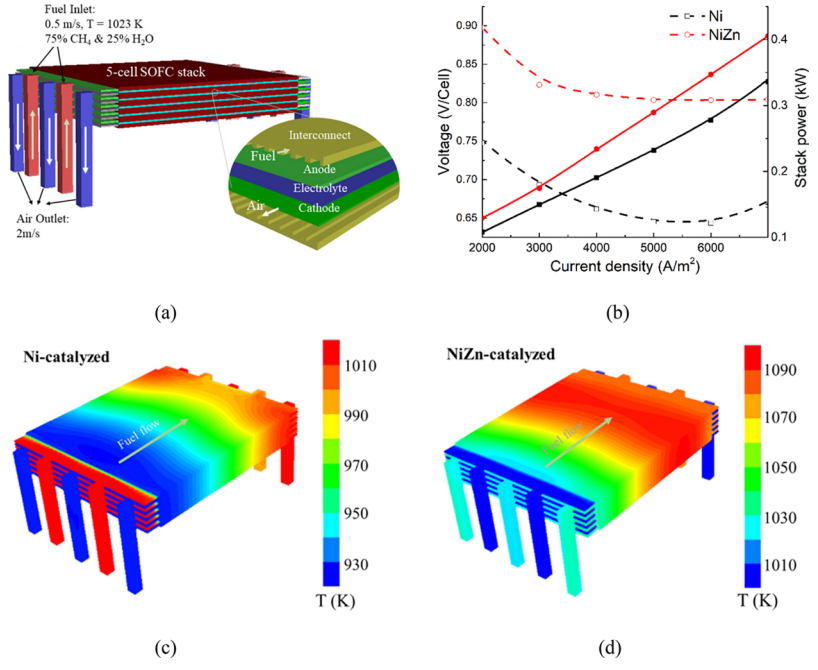

Figure 6. Ni- and NiZn-catalyzed multiphysics SOFC stack modeling. (a) Schematic of the five-cell SOFC model. (b) Current vs voltage (dash lines) and power (solid lines). Temperature distributions (c) for the Ni- and (d) NiZn-catalyzed SOFC.

CONCLUSIONS

We developed a multiscale method of the catalyst design merging top-down and bottom-up approaches, in which microscopic descriptors and multiphysics modeling are bridged by an analytical model, and the descriptors are rapidly predicted by first-principles-based DNNs. This method was used to search for industrial SMR catalysts. The analytical model clearly revealed that C* and O* adsorption energies are key microscopic descriptors for SMR activity and explained the seemingly contradictory activity order of transition metals. Three highly active, low-cost, coke-tolerant, and environment-friendly catalysts, Ni_3Ga, NiZn, and CoGa, were identified from a large database of bimetallic alloys, and their catalytic performances were further confirmed by detailed DFT calculations. Finally, the analytical model was implemented into a multiphysics model, which demonstrated that NiZn, though being less active, turned out to be a better catalyst for the internal reforming solid oxide fuel cell (SOFC), highlighting the importance of the multiphysics model for the multiscale computational catalyst design. We expect that this method can be directly applied to other reactions, promoting the design of new catalysts in the future.

https://doi.org/10.1021/acs.jpcc.1c01632
J. Phys. Chem. C 2021, 125, 10860−10867

■ ASSOCIATED CONTENT

Supporting Information

The Supporting Information is available free of charge at https://pubs.acs.org/doi/10.1021/acs.jpcc.1c01632.

Additional data, including mesh testing, deriving of the analytic equation, linear scaling relationship, validation of the DNN, data of DNN's prediction, and properties of the experimental phase of candidate alloys (PDF)

■ AUTHOR INFORMATION

Corresponding Authors

Shi Liu − *School of Science, Westlake University, Hangzhou, Zhejiang 310024, China; Institute of Natural Sciences, Westlake Institute for Advanced Study, Hangzhou, Zhejiang 310024, China; Key Laboratory for Quantum Materials of Zhejiang Province, Hangzhou, Zhejiang 310024, China;* orcid.org/0000-0002-8488-4848; Email: liushi@westlake.edu.cn

Zijing Lin − *Hefei National Laboratory for Physical Sciences at Microscales & CAS Key Laboratory of Strongly-Coupled Quantum Matter Physics, Department of Physics, University of Science and Technology of China, Hefei 230026, China;* orcid.org/0000-0001-9270-1717; Email: zjlin@ustc.edu.cn

Authors

Changming Ke − *Hefei National Laboratory for Physical Sciences at Microscales & CAS Key Laboratory of Strongly-Coupled Quantum Matter Physics, Department of Physics, University of Science and Technology of China, Hefei 230026, China; School of Science, Westlake University, Hangzhou, Zhejiang 310024, China; Institute of Natural Sciences, Westlake Institute for Advanced Study, Hangzhou, Zhejiang 310024, China;* orcid.org/0000-0002-2018-2441

Weigang He − *Hefei National Laboratory for Physical Sciences at Microscales & CAS Key Laboratory of Strongly-Coupled Quantum Matter Physics, Department of Physics, University of Science and Technology of China, Hefei 230026, China*

Shixue Liu − *System Engineering and Modification Center, China Nuclear Power Technology Research Institute, Shenzhen 518124, China*

Xiao Ru − *Hefei National Laboratory for Physical Sciences at Microscales & CAS Key Laboratory of Strongly-Coupled Quantum Matter Physics, Department of Physics, University of Science and Technology of China, Hefei 230026, China*

Complete contact information is available at: https://pubs.acs.org/10.1021/acs.jpcc.1c01632

Author Contributions

#C.K. and W.H. contributed equally.

Notes

The authors declare no competing financial interest.

All data are available from the corresponding authors upon reasonable request.

■ ACKNOWLEDGMENTS

Z.L. acknowledges the financial support of the National Natural Science Foundation of China (grant nos. 11774324 and 12074362) and the computing time of the Supercomputer Center of the University of Science and Technology of China. C.K. and S.L. acknowledge the support from the Westlake Education Foundation.

■ REFERENCES

(1) Nørskov, J. K.; Bligaard, T.; Rossmeisl, J.; Christensen, C. H. Towards the Computational Design of Solid Catalysts. *Nat. Chem.* **2009**, *1*, 37−46.

(2) Bruix, A.; Margraf, J. T.; Andersen, M.; Reuter, K. First-Principles-Based Multiscale Modelling of Heterogeneous Catalysis. *Nat. Catal.* **2019**, *2*, 659−670.

(3) Li, A.; Song, C.; Lin, Z. J. A Multiphysics Fully Coupled Modeling Tool for the Design and Operation Analysis of Planar Solid Oxide Fuel Cell Stacks. *Appl. Energy* **2017**, *190*, 1234−1244.

(4) Xu, Y.; Lausche, A. C.; Wang, S.; Khan, T. S.; Abild-Pedersen, F.; Studt, F.; Nørskov, J. K.; Bligaard, T. In Silico Search for Novel Methane Steam Reforming Catalysts. *New J. Phys.* **2013**, *15*, 125021−125036.

(5) Matera, S.; Blomberg, S.; Hoffmann, M. J.; Zetterberg, J.; Gustafson, J.; Lundgren, E.; Reuter, K. Evidence for the Active Phase of Heterogeneous Catalysts through in Situ Reaction Product Imaging and Multiscale Modeling. *ACS Catal.* **2015**, *5*, 4514−4518.

(6) Gu, G. H.; Choi, C.; Lee, Y.; Situmorang, A. B.; Noh, J.; Kim, Y. H.; Jung, Y. Progress in Computational and Machine-Learning Methods for Heterogeneous Small-Molecule Activation. *Adv. Mater.* **2020**, *32*, 1907865−1907894.

(7) Vojvodic, A.; Nørskov, J. K. New Design Paradigm for Heterogeneous Catalysts. *Natl. Sci. Rev.* **2015**, *2*, 140−143.

(8) Xin, H.; Holewinski, A.; Schweitzer, N.; Nikolla, E.; Linic, S. Electronic Structure Engineering in Heterogeneous Catalysis: Identifying Novel Alloy Catalysts Based on Rapid Screening for Materials with Desired Electronic Properties. *Top. Catal.* **2012**, *55*, 376−390.

(9) Ma, X.; Li, Z.; Achenie, L. E. K.; Xin, H. Machine-Learning-Augmented Chemisorption Model for Co2 Electroreduction Catalyst Screening. *J. Phys. Chem. Lett.* **2015**, *6*, 3528−3533.

(10) Li, Z.; Ma, X.; Xin, H. Feature Engineering of Machine-Learning Chemisorption Models for Catalyst Design. *Catal. Today* **2017**, *280*, 232−238.

(11) Li, Z.; Wang, S.; Chin, W. S.; Achenie, L. E.; Xin, H. High-Throughput Screening of Bimetallic Catalysts Enabled by Machine Learning. *J. Mater. Chem. A* **2017**, *5*, 24131−24138.

(12) Butler, K. T.; Davies, D. W.; Cartwright, H.; Isayev, O.; Walsh, A. Machine Learning for Molecular and Materials Science. *Nature* **2018**, *559*, 547−555.

(13) Gasper, R.; Shi, H.; Ramasubramaniam, A. Adsorption of Co on Low-Energy, Low-Symmetry Pt Nanoparticles: Energy Decomposition Analysis and Prediction Via Machine-Learning Models. *J. Phys. Chem. C* **2017**, *121*, 5612−5619.

(14) Jinnouchi, R.; Asahi, R. Predicting Catalytic Activity of Nanoparticles by a Dft-Aided Machine-Learning Algorithm. *J. Phys. Chem. Lett.* **2017**, *8*, 4279−4283.

(15) Wexler, R. B.; Martirez, J. M. P.; Rappe, A. M. Chemical Pressure-Driven Enhancement of the Hydrogen Evolving Activity of Ni2p from Nonmetal Surface Doping Interpreted Via Machine Learning. *J. Am. Chem. Soc.* **2018**, *140*, 4678−4683.

(16) Goodfellow, I.; Bengio, Y.; Courville, A., *Deep Learning*; MIT Press, 2016.

(17) Ryan, K.; Lengyel, J.; Shatruk, M. Crystal Structure Prediction Via Deep Learning. *J. Am. Chem. Soc.* **2018**, *140*, 10158−10168.

(18) Ghosh, K.; Stuke, A.; Todorović, M.; Jørgensen, P. B.; Schmidt, M. N.; Vehtari, A.; Rinke, P. Deep Learning Spectroscopy: Neural Networks for Molecular Excitation Spectra. *Adv. Sci.* **2019**, *6*, 1801367.

(19) Goh, G. B.; Hodas, N. O.; Vishnu, A. Deep Learning for Computational Chemistry. *J. Comput. Chem.* **2017**, *38*, 1291−1307.

(20) Mater, A. C.; Coote, M. L. Deep Learning in Chemistry. *J. Chem. Inf. Model.* **2019**, *59*, 2545−2559.

(21) Li, H.; Zhang, Z.; Liu, Z. Application of Artificial Neural Networks for Catalysis: A Review. *Catalysts* **2017**, *7*, 306.

(22) Kresse, G.; Hafner, J. Ab Initiomolecular Dynamics for Liquid Metals. *Phys. Rev. B* **1993**, *47*, 558−561.
(23) Kresse, G.; Hafner, J. Ab Initiomolecular-Dynamics Simulation of the Liquid-Metal−Amorphous-Semiconductor Transition in Germanium. *Phys. Rev. B* **1994**, *49*, 14251−14269.
(24) Kresse, G.; Furthmüller, J. Efficiency of Ab-Initio Total Energy Calculations for Metals and Semiconductors Using a Plane-Wave Basis Set. *Comp Mater Sci* **1996**, *6*, 15−50.
(25) Kresse, G.; Furthmüller, J. Efficient Iterative Schemes for Ab Initio Total-Energy Calculations Using a Plane-Wave Basis Set. *Phys. Rev. B* **1996**, *54*, 11169−11186.
(26) Klimes, J.; Bowler, D. R.; Michaelides, A. Chemical Accuracy for the Van Der Waals Density Functional. *J. Phys.: Condens. Matter* **2010**, *22*, No. 022201.
(27) Klimes, J.; Bowler, D. R.; Michaelides, A. Van Der Waals Density Functionals Applied to Solids. *Phys. Rev. B* **2011**, *83*, 195131.
(28) Kresse, G.; Joubert, D. From Ultrasoft Pseudopotentials to the Projector Augmented-Wave Method. *Phys. Rev. B* **1999**, *59*, 1758−1775.
(29) Blochl, P. E. Projector Augmented-Wave Method. *Phys. Rev. B* **1994**, *50*, 17953−17979.
(30) Henkelman, G.; Jónsson, H. Improved Tangent Estimate in the Nudged Elastic Band Method for Finding Minimum Energy Paths and Saddle Points. *J. Chem. Phys.* **2000**, *113*, 9978−9985.
(31) Henkelman, G.; Uberuaga, B. P.; Jónsson, H. A Climbing Image Nudged Elastic Band Method for Finding Saddle Points and Minimum Energy Paths. *J. Chem. Phys.* **2000**, *113*, 9901−9904.
(32) Henkelman, G.; Jónsson, H. A Dimer Method for Finding Saddle Points on High Dimensional Potential Surfaces Using Only First Derivatives. *J. Chem. Phys.* **1999**, *111*, 7010−7022.
(33) Chaubey, R.; Sahu, S.; James, O. O.; Maity, S. A Review on Development of Industrial Processes and Emerging Techniques for Production of Hydrogen from Renewable and Sustainable Sources. *Renew. Syst. Energ. Rev.* **2013**, *23*, 443−462.
(34) Chollet, F. *Keras*. https://github.com/keras-team/keras.
(35) Kingma, D. P.; Ba, J. Adam: A Method for Stochastic Optimization. *arXiv preprint arXiv:1412.6980* 2014.
(36) Li, A.; Lin, Z. Efficient Mass Transport and Electrochemistry Coupling Scheme for Reliable Multiphysics Modeling of Planar Solid Oxide Fuel Cell Stack. *Chin. J. Chem. Phys.* **2017**, *30*, 139−146.
(37) Ke, C.; Lin, Z. Elementary Reaction Pathway Study and a Deduced Macrokinetic Model for the Unified Understanding of Ni-Catalyzed Steam Methane Reforming. *React. Chem. Eng.* **2020**, *5*, 873−885.
(38) Blaylock, D. W.; Ogura, T.; Green, W. H.; Beran, G. J. O. Computational Investigation of Thermochemistry and Kinetics of Steam Methane Reforming on Ni(111) under Realistic Conditions. *J. Phys. Chem. C* **2009**, *113*, 4898−4908.
(39) Abild-Pedersen, F.; Greeley, J.; Studt, F.; Rossmeisl, J.; Munter, T. R.; Moses, P. G.; Skulason, E.; Bligaard, T.; Norskov, J. K. Scaling Properties of Adsorption Energies for Hydrogen-Containing Molecules on Transition-Metal Surfaces. *Phys. Rev. Lett.* **2007**, *99*, No. 016105.
(40) Michaelides, A.; Liu, Z. P.; Zhang, C. J.; Alavi, A.; King, D. A.; Hu, P. Identification of General Linear Relationships between Activation Energies and Enthalpy Changes for Dissociation Reactions at Surfaces. *J. Am. Chem. Soc.* **2003**, *125*, 3704−3705.
(41) Rostrup-nielsen, J. R.; Hansen, J. H. B. Co2-Reforming of Methane over Transition Metals. *J. Catal.* **1993**, *144*, 38−49.
(42) Kikuchi, E.; Tanaka, S.; Yamazaki, Y.; Morita, Y. Steam Reforming of Hydrocarbons on Noble Metal Catalysts (Part 1). *Bulletin of the Japan Petroleum Institute* **1974**, *16*, 95−98.
(43) Su, X.; Tedenac, J.-C. Thermodynamic Modeling of the Cobalt−Gallium System. *Intermetallics* **2005**, *13*, 467−473.
(44) Jedličková, V.; Zemanová, A.; Kroupa, A. The Thermodynamic Assessment of the Co-Sn System. *J. Phase Equilib. Diffus.* **2018**, *40*, 21−33.
(45) Vassilev, G. P.; Jiang, M. Thermodynamic Optimization of the Co-Zn System. *J. Phase Equilib. Diffus.* **2004**, *25*, 259−268.
(46) Ducher, R.; Kainuma, R.; Ishida, K. Phase Equilibria in the Ni-Rich Portion of the Ni−Ga Binary System. *Intermetallics* **2007**, *15*, 148−153.
(47) Nash, P.; Nash, A. The Ni-Sn (Nickel-Tin) System. *Bulletin of alloy phase diagrams* **1985**, *6*, 350−359.
(48) Su, X.; Tang, N. Y.; Toguri, J. M. Thermodynamic Assessment of the Ni-Zn System. *J. Phase Equilib.* **2001**, *23*, 140−148.
(49) Kumar, K. C. H.; Wollants, P.; Delaey, L. Thermodynamic Evaluation of Fe-Sn Phase Diagram. *Calphad* **1996**, *20*, 139−149.
(50) Xiao, J.; Xie, Y.; Liu, J.; Liu, M. Deactivation of Nickel-Based Anode in Solid Oxide Fuel Cells Operated on Carbon-Containing Fuels. *J. Power Sources* **2014**, *268*, 508−516.
(51) Zuo, P.; Fu, Z.; Yang, Z. First-Principles Study on the Mechanism of Coking Inhibition by the Ni(111) Surface Doped with Ib-Group Metals at the Anode of Solid Oxide Fuel Cells. *J. Power Sources* **2013**, *242*, 762−767.
(52) Fan, M.-S.; Abdullah, A. Z.; Bhatia, S. Utilization of Greenhouse Gases through Carbon Dioxide Reforming of Methane over Ni−Co/Mgo−Zro2: Preparation, Characterization and Activity Studies. *Appl. Catal., B* **2010**, *100*, 365−377.
(53) San-José-Alonso, D.; Juan-Juan, J.; Illán-Gómez, M. J.; Román-Martínez, M. C. Ni, Co and Bimetallic Ni−Co Catalysts for the Dry Reforming of Methane. *Appl. Catal., A* **2009**, *371*, 54−59.
(54) Liu, J.; Peng, H.; Liu, W.; Xu, X.; Wang, X.; Li, C.; Zhou, W.; Yuan, P.; Chen, X.; Zhang, W.; et al. Tin Modification on Ni/Al2o3: Designing Potent Coke-Resistant Catalysts for the Dry Reforming of Methane. *ChemCatChem* **2014**, *6*, 2095−2104.
(55) Nikolla, E.; Holewinski, A.; Schwank, J.; Linic, S. Controlling Carbon Surface Chemistry by Alloying: Carbon Tolerant Reforming Catalyst. *J. Am. Chem. Soc.* **2006**, *128*, 11354−11355.
(56) Nieva, M. A.; Villaverde, M. M.; Monzón, A.; Garetto, T. F.; Marchi, A. J. Steam-Methane Reforming at Low Temperature on Nickel-Based Catalysts. *Chem. Eng. J.* **2014**, *235*, 158−166.
(57) Studt, F.; Abild-Pedersen, F.; Bligaard, T.; Sorensen, R. Z.; Christensen, C. H.; Norskov, J. K. Identification of Non-Precious Metal Alloy Catalysts for Selective Hydrogenation of Acetylene. *Science* **2008**, *320*, 1320−1322.
(58) Kwak, B. S.; Lee, J. S.; Lee, J. S.; Choi, B.-H.; Ji, M. J.; Kang, M. Hydrogen-Rich Gas Production from Ethanol Steam Reforming over Ni/Ga/Mg/Zeolite Y Catalysts at Mild Temperature. *Appl. Energy* **2011**, *88*, 4366−4375.
(59) Andersson, M. P.; Bligaard, T.; Kustov, A.; Larsen, K. E.; Greeley, J.; Johannessen, T.; Christensen, C. H.; Nørskov, J. K. Toward Computational Screening in Heterogeneous Catalysis: Pareto-Optimal Methanation Catalysts. *J. Catal.* **2006**, *239*, 501−506.
(60) Okamoto, H. The Fe-Ga (Iron-Gallium) System. *Bulletin of alloy phase diagrams* **1990**, *11*, 576−581.
(61) Singh, D.; Suryanarayana, C.; Mertus, L.; Chen, R. H. Extended Homogeneity Range of Intermetallic Phases in Mechanically Alloyed Mg−Al Alloys. *Intermetallics* **2003**, *11*, 373−376.
(62) Claridge, J. B.; Green, M. L. H.; Tsang, S. C.; York, A. P. E.; Ashcroft, A. T.; Battle, P. D. A Study of Carbon Deposition on Catalysts During the Partial Oxidation of Methane to Synthesis Gas. *Catal. Lett.* **1993**, 299.
(63) Fang, X.; Lin, Z. Numerical Study on the Mechanical Stress and Mechanical Failure of Planar Solid Oxide Fuel Cell. *Appl. Energy* **2018**, *229*, 63−68.

https://doi.org/10.1021/acs.jpcc.1c01632
J. Phys. Chem. C 2021, 125, 10860−10867